

Intrinsic Alignments and Splashback Radius of Dark Matter Halos from Cosmic Density and Velocity Fields

Tepppei Okumura,^{1,*} Takahiro Nishimichi,^{2,3} Keiichi Umetsu,¹ and Ken Osato⁴

¹*Institute of Astronomy and Astrophysics, Academia Sinica, P. O. Box 23-141, Taipei 10617, Taiwan*

²*Kavli Institute for the Physics and Mathematics of the Universe (WPI),*

UTIAS, The University of Tokyo, Kashiwa, Chiba 277-8583, Japan

³*CREST, JST, 4-1-8 Honcho, Kawaguchi, Saitama, 332-0012, Japan*

⁴*Department of Physics, University of Tokyo, 7-3-1 Hongo, Bunkyo-ku, Tokyo 113-0033 Japan*

(Dated: May 29, 2022)

We investigate the effects of intrinsic alignments (IA) of dark-matter halo shapes on cosmic density and velocity fields from cluster to cosmic scales beyond $100 h^{-1}$ Mpc. Besides the density correlation function binned by the halo orientation angle which was used in the literature, we introduce, for the first time, the corresponding two velocity statistics, the angle-binned pairwise infall momentum and momentum correlation function. Using large-volume, high-resolution N -body simulations, we measure the alignment statistics of density and velocity, both in real and redshift space. We find that the alignment signal is not amplified by redshift-space distortions at linear scales. Behaviors of IA in the velocity statistics are similar to those in the density statistics, except that the halo orientations are aligned with the velocity field up to a scale larger than those with the density field, $x > 100 h^{-1}$ Mpc. On halo scales, $x \sim R_{200m} \sim 1 h^{-1}$ Mpc, we detect a sharp steepening in the momentum correlation associated with the physical halo boundary, or the splashback feature, which is found more prominent than in the density correlation. Our results indicate that observations of IA with the velocity field can provide additional information on cosmological models from large scales and on physical sizes of halos from small scales.

Introduction.— Intrinsic alignments (IA) of galaxy images in principle contain useful information to probe the galaxy formation processes. Detailed studies of IA are also important on large scales since it can act as contamination when the shape information is used in weak lensing surveys for precision cosmology. The effects of this contamination have been actively studied both theoretically [1, 2] and observationally [3–6] (See, e.g., [7, 8] for reviews). More interestingly, this IA effect is known to depend strongly on the mass of host dark-matter halos [9]. Thanks to robust and efficient cluster-finding algorithms recently developed based on the observed galaxy distribution [10, 11], strong alignment signals have been detected up to scales larger than $100 h^{-1}$ Mpc [12, 13]. Galaxy clusters are thus ideal objects to address a fundamental question of up to what scales luminous objects are aligned with the matter distribution in the large-scale structure of the universe. Moreover, clusters enable us to investigate intra-halo structure by cross-correlating with galaxies in and around the clusters. Here, of particular interest is the identification and characterization of physical boundaries of halos by studying splashback features associated with the outermost caustic in accreting halos [14–16]. The goal of this study is to simultaneously investigate the splashback features and IA of clusters.

In past work, alignments of the major axes of galaxies relative to the overdensity field have been studied when IA were investigated. However, it is fundamentally important to consider the IA relative to the cosmic velocity field with various reasons. Now the velocity field at cosmic scales can be measured through several ways, such as peculiar velocity [17] and kinematic Sunyaev-Zel’dovich

(kSZ) [18] surveys. Since the velocity field in Fourier space follows $\mathbf{v}_{\mathbf{k}} \propto (i\mathbf{k}/k^2)\delta_{\mathbf{k}}$ in linear theory, one expects that the velocity correlation signal is amplified compared to the density counterpart on large scales. This trend has been seen in the measured pairwise velocity power spectrum in kSZ surveys [19, 20]. In this paper we introduce new statistics, namely the alignment velocity statistics. We formulate the two alignment velocity statistics, and using the high-resolution N -body simulations, we test the statistics over a broad range of scales, from a 1-halo regime to the scale beyond $100 h^{-1}$ Mpc.

Alignment correlation function.— The statistic commonly used to quantify IA in a weak-lensing context is the gravitational shear–intrinsic ellipticity (GI) correlation functions [2]. In this work, we consider an alternative quantity, namely the angle-binned or alignment correlation function [21] [47]. It is defined as an extension of the conventional two-point correlation function of the two fields A and B , $\xi_{AB}(\mathbf{x}) = \langle \delta_A(\mathbf{r}_1)\delta_B(\mathbf{r}_2) \rangle$, where $\mathbf{x} = \mathbf{r}_2 - \mathbf{r}_1$ [48]. The alignment correlation function is expressed as functions of \mathbf{x} and the angle between the elongated orientation of the matter field, traced by the major axes of halo or galaxy shapes, and \mathbf{x} projected onto the sky, θ , so that $\xi_{AB}(\mathbf{x}, \theta) = \langle \delta_A(\mathbf{r}_1)\delta_B(\mathbf{r}_2, \theta) \rangle$. The conventional correlation function can be obtained by integrating over θ , $\xi_{AB}(\mathbf{x}) = (2/\pi) \int_0^{\pi/2} d\theta \xi_{AB}(\mathbf{x}, \theta)$. Since the distances to objects are measured through redshift in galaxy surveys, the correlation function is affected by their velocities and becomes anisotropic, known as redshift-space distortions (RSD) [22]. In linear perturbation theory of the density field, RSD produce the quadrupole and hexadecapole moments in addition to the

monopole. In this paper we consider only the monopole, $\xi_{AB,0}(x, \theta) = \int_0^1 d\mu \xi_{AB}(\mathbf{x}, \theta)$, where μ is the direction cosign between the vector \mathbf{x} and the line of sight \mathbf{r} , $\mu = \hat{\mathbf{x}} \cdot \hat{\mathbf{r}}$, where the hat denotes a unit vector. Throughout this paper we assume the distant observer approximation, so that $\hat{\mathbf{r}}_1 = \hat{\mathbf{r}}_2 \equiv \hat{\mathbf{r}}$. Hereafter we omit the subscript 0 which represents the monopole moment and simply write $\xi_{AB}(x, \theta)$.

The GI correlation function to quantify the IA effect on the weak-lensing shear power spectrum is expressed as $\xi_{A+}(\mathbf{x}) = \langle \delta_A(\mathbf{r}_1) \gamma^I(\mathbf{r}_2) \rangle$, where $\gamma^I(\mathbf{r}) = q \cos(2\theta)$ and q is a weight factor of the major-to-minor-axis ratio. The GI function corresponds to the dipole moment of the alignment correlation function, $\tilde{\xi}_{A+}(\mathbf{x}) = (2/\pi) \int_0^{\pi/2} d\theta \cos(2\theta) \xi_{AB}(\mathbf{x}, \theta)$, where $\tilde{\xi}_{A+}$ is the same as ξ_{A+} but with q fixed to $q = 1$ [21, 23].

Alignment velocity statistics.— In this paper we extend the alignment density statistics and consider the alignment of halos/galaxies relative to the cosmic velocity field. Here we consider two types of the velocity statistics [24–26]. One is the pairwise mean momentum: $p_{AB}(\mathbf{x}) = \langle [1 + \delta_A(\mathbf{r}_1)] [1 + \delta_B(\mathbf{r}_2)] [v_A^z(\mathbf{r}_1) - v_B^z(\mathbf{r}_2)] \rangle$, where $v_A^z(\mathbf{r})$ is the radial component of the peculiar velocity of sample A , $v_A^z(\mathbf{r}) = \mathbf{v}_A(\mathbf{r}) \cdot \hat{\mathbf{r}}$. Another statistics is the momentum correlation function: $\psi_{AB}(\mathbf{x}) = \langle [1 + \delta_A(\mathbf{r}_1)] [1 + \delta_B(\mathbf{r}_2)] v_A^z(\mathbf{r}_1) v_B^z(\mathbf{r}_2) \rangle$. Note that in observations such as peculiar velocity and kSZ survey data, the velocity field is also sampled in redshift space, thus affected by RSD, as formulated by [26, 27] in detail.

We define the angle-binned pairwise infall momentum, $p_{AB}(\mathbf{x}, \theta)$, and momentum correlation function, $\psi_{AB}(\mathbf{x}, \theta)$, by replacing $\delta_B(\mathbf{r}_2)$ in the above equations by $\delta_B(\mathbf{r}_2, \theta)$ [49]. In a similar manner to the density correlation function, the conventional expression for these velocity statistics, $p_{AB}(\mathbf{x})$ and $\psi_{AB}(\mathbf{x})$, can be obtained by averaging over θ . These are the main statistics we will study in this paper. We will focus only on the lowest-order moments of these statistics, namely the dipole moment of the pairwise momentum and the monopole moment of the momentum correlation function, $p_{AB}(x, \theta) = 3 \int_0^1 d\mu \mu p_{AB}(\mathbf{x}, \theta)$ and $\psi_{AB}(x, \theta) = \int_0^1 d\mu \psi_{AB}(\mathbf{x}, \theta)$, respectively. The effects of IA on the higher-order moments will be studied in our future work.

N-body simulations.— In order to study the density and velocity alignment statistics, we use a series of large and high-resolution N -body simulations of the Λ CDM cosmology seeded with Gaussian initial conditions. These are performed as a part of the **dark emulator** project (Nishimichi et al. in prep.). We adopt the cosmological parameters of $\Omega_m = 1 - \Omega_\Lambda = 0.315$, $\Omega_b = 0.0492$, $h = 0.673$, $n_s = 0.965$, and $\sigma_8 = 0.8309$. We employ $n_p = 2048^3$ particles of mass $m_p = 8.15875 \times 10^{10} M_\odot/h$ in a cubic box of side $L_{\text{box}} = 2h \text{ Gpc}^{-1}$. We use 4 realizations in total, and analyze the snapshots at $z = 0306$, which will be quoted as $z = 0.3$ in the following.

TABLE I: Properties of mock halo/subhalo samples at $z = 0.3$. f_{sat} is the number fraction of satellites, M_{min} and \bar{M} are the minimum and average halo mass in units of $10^{12} h^{-1} M_\odot$, respectively, and \bar{n} is the number density in units of $h^3 \text{ Mpc}^{-3}$.

halo types	f_{sat}	M_{min}	\bar{n}	b	\bar{M}
Clusters (halos)	0	100	2.05×10^{-5}	3.05	188
Galaxies (subhalos)	0.137	1.63	5.27×10^{-4}	1.69	25.2

Halos and subhalos are identified using phase-space information of The velocity of a *Rockstar* (sub)halo is determined by the The velocity of the (sub)halo is determined by the average particle velocity within the innermost 10% of the (sub)halo radius. We use the standard definition for the halo radius and mass of $M_h \equiv M_{\Delta m} = M(< R_{\Delta m}) = (4\pi/3) \Delta m \rho_m(z) R_{\Delta m}^3$, with ρ_m the mean mass density of the universe at given redshift z , and we adopt $\Delta m = 200$. To study cluster-scale halos, we select halos with $M_h \geq 10^{14} h^{-1} M_\odot$, which roughly corresponds to the typical threshold of the richness parameters used by the cluster-finding algorithms in the literature. We will mainly present the analysis of IA of the cluster shapes relative to the density field traced by galaxies. To this end, we create mock galaxy catalogs using a halo occupation distribution (HOD) model [29] applied for the LOWZ galaxy sample of the SDSS-III Baryon Oscillation Spectroscopic Survey (BOSS) obtained by [30]. We populate halos with galaxies according to the best-fitting HOD $N(M_h)$. For halos that contain satellite galaxies, we randomly draw $N(M_h) - 1$ member subhalos to mimic the positions and velocities of the satellites The HOD modeling of the BOSS galaxy samples is known to overestimate the number density by $\sim 30 - 40\%$. Since the purpose of this study is not to create an accurate galaxy sample, this issue does not affect any of our final results and conclusions. See [31, 32] for the methods of creating a galaxy catalog based on N -body subhalo catalogs. We assume halos to have triaxial shapes and estimate the orientations of their major axes using the second moments of the mass distribution projected onto the celestial plane. Table I summarizes properties of our mock galaxy and cluster samples.

Estimators.— In observational studies of IA in weak-lensing surveys, one usually considers a correlation function projected along the line of sight. Thus, the contributions of RSD are largely cancelled out, while the IA signal is also smeared out to some extent by projection effects. Since we are interested in the IA signal itself, we present the alignment density and velocity correlation statistics in both real space and redshift space.

The alignment correlation function of the density (A) and shape (B) samples can be measured by $\xi_{AB}(x, \theta) = \langle D_A D_B \rangle / \langle R_A R_B \rangle - 1$, where $\langle D_A D_B \rangle(x, \theta)$ is the normalized pair count of the samples as functions of sep-

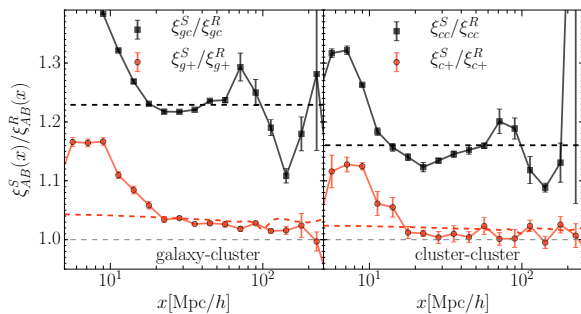


FIG. 1: Ratio of GI correlation functions in redshift and real space for galaxy-cluster (left) and cluster-cluster (right), shown as the red points. The corresponding ratios of the density correlations are shown as the black points. The horizontal black and red lines are the predictions of the Kaiser formula for the density and GI correlation functions, respectively.

aration x and angle θ . $\langle R_A R_B \rangle(x, \theta)$ is the the same as $\langle D_A D_B \rangle(x, \theta)$ but the two samples are randomly distributed. The momentum correlation function can be measured by a simple estimator: $\psi_{AB}(x, \theta) = \langle V_A^z V_B^z \rangle / \langle R_A R_B \rangle$, where $\langle V_A^z V_B^z \rangle(x, \theta)$ is the normalized pair count of Samples A and B weighted by the products of the radial components of their velocities as functions of x and θ . We adopt an estimator for the pairwise momentum dipole [26], $p_{AB}(x, \theta) = \langle (V_A^z D_B - D_A V_B^z) \hat{\mathbf{r}} \cdot \hat{\mathbf{x}} \rangle / \langle R_A R_B (\hat{\mathbf{r}} \cdot \hat{\mathbf{x}})^2 \rangle$. This is a modified version of the estimator proposed in [33] who used the number of correlated pairs for the denominator instead of the uncorrelated pairs. In this analysis, the shape information is taken from clusters, so that sample B is always a cluster, $B = \{c\}$, while otherwise stated, the density field A is traced by galaxies, $A = \{g\}$. In the following analysis, we measure these statistics from each of the four realizations and present their means and standard errors from the scatters.

Numerical analysis.— We start by presenting the GI correlation functions in real space and redshift space because the results can be compared to simple analytical predictions [6]. The left panel of Fig. 1 shows the ratio of the GI correlation functions in redshift and real space measured using the estimator of [3]. The right panel shows the result where both the shape and density fields are from the clusters. For comparison, we also show the corresponding ratios of the density correlation functions in redshift and real space. The horizontal black line is the linear prediction of Kaiser formula, $\xi_{AB}^S/\xi_{AB}^R = 1 + (\beta_A + \beta_B)/3 + \beta_A \beta_B/5$, where $AB = \{gc, cc\}$, $\beta_A = f/b_A$, $f = \ln \delta / \ln a$ with a the scale factor, and the superscripts S and R denote the statistics measured in redshift and real space, respectively. The linear bias parameter of Sample A , b_A , is determined from $b_A(x) = (\xi_{AA}^R/\xi_m^R)^{1/2}$ on $20 < x < 80 [h^{-1} \text{ Mpc}]$ where ξ_m^R is the matter correlation function and here we simply compute it using linear theory based on the *CAMB* code

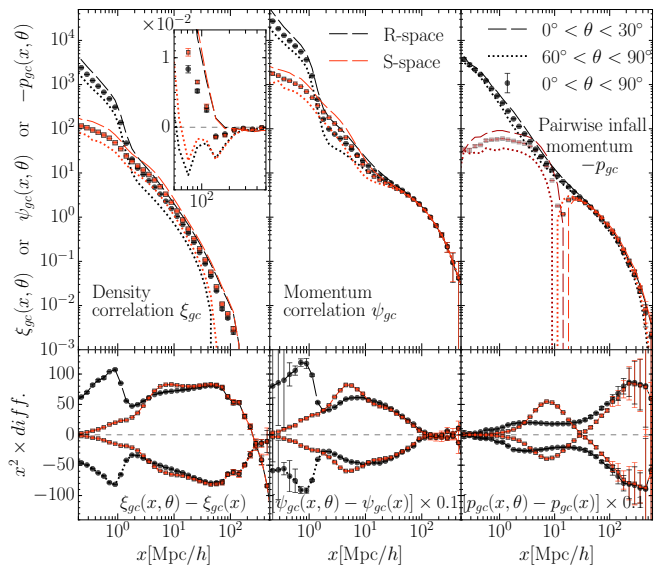


FIG. 2: (Left) Angle-binned density correlation function of galaxy density and cluster orientation in real space (red) and redshift space (black). In the top panel the dashed and dotted lines respectively show the alignment correlations parallel and perpendicular to the major axes of the clusters $\xi_{gc}(x, \theta)$ while the points with error bars the conventional correlation functions, and the bottom panel is their difference, $x^2[\xi_{gc}(x, \theta) - \xi_{gc}(x)]$. The inset provides the zoomed view on large scales. (Center) Angle-binned momentum correlation functions, $\psi_{gc}(x, \theta)$, which have a unit of $[h^{-1} \text{ Mpc}]^2$. In the bottom panel the amplitude is multiplied by 0.1. (Right) Angle-binned pairwise mean infall momentum. Since the statistics has negative values at linear scales, we show $-p_{gc}$ at the top panel, and the points and lines colored darker red are its negative values in redshift space, $-(-p_{gc}^S) = p_{gc}^S$. The amplitude in the bottom panel is multiplied by 0.1.

[34]. The values of the bias are shown in Table I. The red horizontal line is the Kaiser prediction for the redshift-space and real-space ratio for the GI correlation. It gives a reasonable ratio around 1.2 for the density correlation on sufficiently large scales up to $x \sim 125 h^{-1} \text{ Mpc}$, where the correlation function crosses zero. The enhancement of the 3D alignment statistics by RSD is, by contrast, only a few percent for the galaxy-cluster GI, and further suppressed for cluster-cluster GI by the factor f/b . The smaller ratio for the alignment statistics is because of the more complicated oscillatory kernel in the integral. In the following analysis we will show the alignment correlation of density and velocity measured both in real and redshift space, although the alignment signals are expected to be similar according to this result.

In the top-left panel of Fig. 2, we show the cluster-galaxy density cross correlation function binned in θ . Though not presented here, the trend is basically the same for the cluster auto correlation. As expected from Fig. 1, the alignment signals are almost the same on large scales in real and redshift space unlike the density correla-

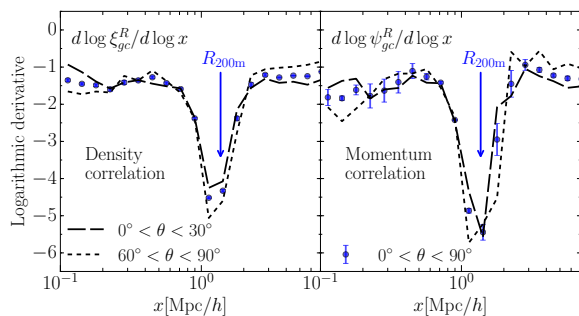


FIG. 3: (Left) Logarithmic slope of the angle-binned density correlation of galaxy density and cluster orientation in real space, $d \log \xi_{gc}^R(x, \theta) / d \log x$. The solid and dotted lines, respectively, are the correlation parallel and perpendicular to the major axes of the clusters, while the blue points with error bars are for the conventional correlation function. The location of R_{200m} , which coincides well with R_{sp} , is denoted by the arrow. (Right) Same as the left panel but for the momentum correlation function.

tion. This signal has been measured both in simulations and observations [5, 35].

On the scale of $x \sim 1 h^{-1}$ Mpc, an abrupt change in the slope of the real-space correlation can be seen, whereas it is washed out in redshift space by the $\sim 10 h^{-1}$ Mpc line-of-sight displacement of galaxies due to RSD. There have been intensive efforts to understand and characterize the physical boundary of halos in terms of the steepest point of the density gradient. The location of this halo boundary is referred to as the splashback radius R_{sp} [14] (See [36] for an alternative approach to define the boundary using the satellite distribution). Here we show the logarithmic slope of the real-space alignment correlation, $\gamma = d \log \xi_{gc}^R / d \log x$, in the left panel of Fig. 3. The steepest slope of our conventional correlation function reaches $\gamma \simeq -4.5$ at $R_{sp} \simeq R_{200m}$, significantly steeper than the asymptotic outer slope (-3) of the standard Navarro–Frenk–White profile [37]. This is consistent with the characteristic splashback properties in Λ CDM found by [14]. Intriguingly, the slopes are shallower and steeper, respectively, for the density alignment correlation parallel and perpendicular to the major axes of the clusters. This can be qualitatively interpreted by the fact that the halo size varies more significantly along the direction of the major axis (i.e., smaller θ), leading to a less prominent boundary. The location of R_{200m} in our sample, which coincides well with the respective steepest gradient point, is denoted by the arrow in the figure. The mean $R_{sp}-R_{200m}$ relation of [38] predicts $R_{sp} = 1.001 R_{200m} \simeq 1.37 h^{-1}$ Mpc for our cluster sample with $\bar{M}_{200m} = 1.88 \times 10^{14} h^{-1} M_{\odot}$, so that it precisely matches the detected splashback scales. It is also interesting to note that the IA signal is further enhanced within the splashback shell, as seen in the left bottom panel of Fig. 2, consistent with the halo model of IA [39].

The next quantity to consider is the angle-binned momentum correlation function. Its numerical results are shown in the upper-middle panel of Fig. 2. On large scales where linear theory holds, the correlation in redshift space is equivalent to that in real space [26]. As seen in the lower-middle panel, the IA signal in the momentum correlation vanishes at $x \sim 100 h^{-1}$ Mpc, on a scale smaller than that of the density correlation. We see a steepening feature of the real-space momentum correlation at $R_{sp} \simeq R_{200m}$, very similar to that of the density correlation. To see the feature in more detail, we show the logarithmic derivative, $\gamma_p = d \log \psi_{gc}^R / d \log x$, in the right panel of Fig. 3. It is interesting to note that the slope approaches $\gamma_p \rightarrow -5.5$, steeper than the boundary slope determined by the density correlation. As discussed by [40] in the context of Λ CDM structure formation, the orbital velocity anisotropy is tightly coupled with the logarithmic density slope around halos and thus expected to be sensitive to the location of the halo edge [14], which physically and sharply separates the multi-stream intra-halo region from the outer infall region (see also [41]). Besides, the splashback feature and the enhancement of IA at this scale are found more prominent for the momentum correlation than for the density correlation. However, since the momentum correlation is noisier than the density correlation, we cannot see a clear dependence of the splashback feature on IA in our simulations.

Finally, we turn to another velocity statistic, the pairwise mean infall momentum. The upper-right panel of Fig. 2 shows the angle-binned pairwise mean momentum. As expected, we do not see a splashback feature from this statistic even in real space. On large scales where linear perturbation theory holds, objects approach each other on average, so that the correlation becomes negative. On the other hand, on small scales, the sign of the redshift-space pairwise momentum changes from negative to positive due to the non-linear velocity dispersion [26, 27]. We note that in the lower-right panel the alignment signal in p_{gc} persists beyond $x \sim 200 h^{-1}$ Mpc.

Outlook.— The presented analysis of IA with the velocity field has several important applications. Recently, an idea of testing inflation models using IA on large scales has been proposed by [42]. The angle-binned pairwise momentum, $p_{AB}(x, \theta)$, or its ratio to the density correlation, $p_{AB}(x, \theta) / \xi_{AB}(x, \theta)$, may serve as a powerful tool to probe inflation. Future kSZ surveys enable us to measure the large-scale velocity field and constrain cosmological models using the higher-order velocity moments [43]. Detailed studies of the velocity IA effect based on the (non)linear alignment and halo models [2, 39, 44], as well as large-volume N -body simulations, will be presented in our future work. A possible contaminant of utilizing the kSZ for probing the velocity field is the effect of the optical depth. However, a promising method of measuring it has recently been proposed based on a semi-analytic technique calibrated with X-ray observa-

tions [45]. Note that to compare simulation results of IA to observations, shapes of brightest cluster galaxies (BCG) are often used as a proxy for the cluster shapes. In this case, the misalignment between the major axes of BCG and their host halos needs to be taken into account [4]. Although the misalignment for such massive halos is known to be small [46], it needs to be studied carefully.

The splashback radius R_{sp} has been detected for the first time in the momentum correlation function from N -body simulations. The feature is even sharper than that in the density correlation, because R_{sp} separates distinct infall and multi-stream regions. High-resolution kSZ observations can be used to directly test this prediction in comparison to the splashback feature observed in the density correlation [15], as well as the dependence of cluster orientations on the splashback radius.

This work was in part supported by MEXT Grant-in-Aid for Scientific Research on Innovative Areas (No. 15H05887, 15H05893, 15K21733, and 15H05892). T.N. acknowledges financial support from JSPS KAKENHI Grant Number 17K14273 and JST CREST Grant Number JPMJCR1414. K.U. acknowledges support from the Ministry of Science and Technology of Taiwan under the grant MOST 103-2112-M-001-030-MY3.

* Electronic address: tokumura@asiaa.sinica.edu.tw

- [1] P. Catelan, M. Kamionkowski, and R. D. Blandford, *Mon. Not. Roy. Astron. Soc.* **320**, L7 (2001)
- [2] C. M. Hirata and U. Seljak, *Phys. Rev. D* **70**, 063526 (2004)
- [3] R. Mandelbaum, C. M. Hirata, M. Ishak, U. Seljak, and J. Brinkmann, *Mon. Not. Roy. Astron. Soc.* **367**, 611 (2006)
- [4] T. Okumura, Y. P. Jing, and C. Li, *Astrophys. J.* **694**, 214 (2009)
- [5] C. Li, Y. P. Jing, A. Faltenbacher, and J. Wang, *Astrophys. J. Lett.* **770**, L12 (2013)
- [6] S. Singh, R. Mandelbaum, and S. More, *Mon. Not. Roy. Astron. Soc.* **450**, 2195 (2015)
- [7] B. M. Schäfer, *International Journal of Modern Physics D* **18**, 173 (2009)
- [8] M. A. Troxel and M. Ishak, *Phys. Rept.* **558**, 1 (2015)
- [9] Y. P. Jing, *Mon. Not. Roy. Astron. Soc.* **335**, L89 (2002)
- [10] E. S. Rykoff, et al., *Astrophys. J.* **785**, 104 (2014)
- [11] M. Oguri, *Mon. Not. Roy. Astron. Soc.* **444**, 147 (2014)
- [12] E. van Uitert and B. Joachimi, *Mon. Not. Roy. Astron. Soc.* **468**, 4502 (2017)
- [13] H.-J. Huang, R. Mandelbaum, P. E. Freeman, Y.-C. Chen, E. Rozo, and E. Rykoff, *ArXiv e-prints* (2017), 1704.06273.
- [14] B. Diemer and A. V. Kravtsov, *Astrophys. J.* **789**, 1 (2014)
- [15] S. More, et al., *Astrophys. J.* **825**, 39 (2016)
- [16] K. Umetsu and B. Diemer, *Astrophys. J.* **836**, 231 (2017)
- [17] M. A. Strauss and J. A. Willick, *Phys. Rept.* **261**, 271 (1995)
- [18] N. Hand, et al., *Phys. Rev. Lett.* **109**, 041101 (2012)
- [19] F. De Bernardis, et al., *J. Cosmol. Astropart. Phys.* **3**, 008 (2017)
- [20] N. S. Sugiyama, T. Okumura, and D. N. Spergel, *ArXiv e-prints* (2017), 1705.07449.
- [21] A. Faltenbacher, C. Li, S. D. M. White, Y.-P. Jing, S. Mao, and J. Wang, *Res. Astron. Astrophys.* **9**, 41 (2009)
- [22] N. Kaiser, *Mon. Not. Roy. Astron. Soc.* **227**, 1 (1987).
- [23] T. Okumura and Y. P. Jing, *Astrophys. J. Lett.* **694**, L83 (2009)
- [24] K. Gorski, *Astrophys. J. Lett.* **332**, L7 (1988).
- [25] K. B. Fisher, *Astrophys. J.* **448**, 494 (1995)
- [26] T. Okumura, U. Seljak, Z. Vlah, and V. Desjacques, *J. Cosmol. Astropart. Phys.* **5**, 003 (2014)
- [27] N. S. Sugiyama, T. Okumura, and D. N. Spergel, *J. Cosmol. Astropart. Phys.* **7**, 001 (2016)
- [28] P. S. Behroozi, R. H. Wechsler, and H.-Y. Wu, *Astrophys. J.* **762**, 109 (2013)
- [29] Z. Zheng, et al., *Astrophys. J.* **633**, 791 (2005)
- [30] J. K. Parejko, et al., *Mon. Not. Roy. Astron. Soc.* **429**, 98 (2013)
- [31] T. Nishimichi and A. Oka, *Mon. Not. Roy. Astron. Soc.* **444**, 1400 (2014)
- [32] T. Okumura, M. Takada, S. More, and S. Masaki, *Mon. Not. Roy. Astron. Soc.* **469**, 459 (2017)
- [33] P. G. Ferreira, R. Juszkiewicz, H. A. Feldman, M. Davis, and A. H. Jaffe, *Astrophys. J. Lett.* **515**, L1 (1999)
- [34] A. Lewis, A. Challinor, and A. Lasenby, *Astrophys. J.* **538**, 473 (2000)
- [35] M. D. Schneider, C. S. Frenk, and S. Cole, *J. Cosmol. Astropart. Phys.* **5**, 030 (2012)
- [36] T. Okumura, N. Hand, U. Seljak, Z. Vlah, and V. Desjacques, *Phys. Rev. D* **92**, 103516 (2015)
- [37] J. F. Navarro, C. S. Frenk, and S. D. M. White, *Astrophys. J.* **462**, 563 (1996)
- [38] B. Diemer, P. Mansfield, A. V. Kravtsov, and S. More, *ArXiv e-prints* (2017), 1703.09716.
- [39] M. D. Schneider and S. Bridle, *Mon. Not. Roy. Astron. Soc.* **402**, 2127 (2010)
- [40] A. Lapi and A. Cavaliere, *Astrophys. J.* **692**, 174 (2009)
- [41] A. Faltenbacher and S. D. M. White, *Astrophys. J.* **708**, 469 (2010)
- [42] F. Schmidt, N. E. Chisari, and C. Dvorkin, *J. Cosmol. Astropart. Phys.* **10**, 032 (2015)
- [43] N. S. Sugiyama, T. Okumura, and D. N. Spergel, *J. Cosmol. Astropart. Phys.* **1**, 057 (2017)
- [44] J. Blazek, M. McQuinn, and U. Seljak, *J. Cosmol. Astropart. Phys.* **5**, 10 (2011)
- [45] S. Flender, D. Nagai, and M. McDonald, *Astrophys. J.* **837**, 124 (2017)
- [46] G. Despali, C. Giocoli, M. Bonamigo, M. Limousin, and G. Tormen, *Mon. Not. Roy. Astron. Soc.* **466**, 181 (2017)
- [47] We use the term “angle” to indicate the projected angle θ instead of the direction with regard to the line of sight.
- [48] Here we consider a general case where the two fields are different, e.g., A and B are the fields traced by galaxies and galaxy clusters, respectively, but the expression for the auto correlation can be obtained by setting $A = B$.
- [49] We also defined the the angle-binned density-momentum cross correlation, $\langle [1 + \delta_A(\mathbf{r}_1)] [1 + \delta_B(\mathbf{r}_2, \theta)] v_A^z(\mathbf{r}_1) \rangle$, and angle-binned, pair-weighted velocity dispersion, $\langle [1 + \delta_A(\mathbf{r}_1)] [1 + \delta_B(\mathbf{r}_2, \theta)] (v_A^z(\mathbf{r}_1) - v_B^z(\mathbf{r}_2))^2 \rangle$, and investigated their properties. The behaviors of IA in the former and latter statistics were, however, found to be almost the same as those in p_{AB} and ψ_{AB} , respectively.

